



# Distributed Electric Propulsion Effects on Traditional Aircraft Through Multidisciplinary Optimization

Kevin R. Moore\* and Andrew Ning†

Brigham Young University, Provo, UT, 84602, USA

Electric aircraft face a steep tradeoff between the demand for runway performance and range. While fuel based propulsion technologies typically increase in specific power with increasing size, electric propulsion is typically much more scalable. This system scalability enables alternative designs including distributed propulsion, optionally powered propulsion units, and vectored thrust, which can all contribute to better runway performance and range. In this paper, we explore how continuously powered distributed propulsion can reduce takeoff distance while still satisfying range constraints. We use a combination of a blade element momentum method, a vortex lattice method, experimental data, and nonlinear optimization techniques to model and explore the design space. We have found that for this conceptual design study, a fully blown wing with propellers at the optimal diameter for the load (8 propellers for a 300 km range constraint) can reduce the takeoff distance by over 80% when compared to the optimal 2 propeller case using the same models. There is over a 2x increase in the wing lift coefficient which leads to a 36% reduction in liftoff speed. Also, the optimal fully blown case produced 2.9 more thrust during takeoff with only an 11% increase in total aircraft mass. Using propeller tip speed as a surrogate for noise, we found that the propeller tip speed decreased takeoff performance in an exponential manner: the tip speed could be decreased from Mach 0.8 to Mach 0.5 with only a 2x increase in takeoff rolling distance while decreasing the constraint to Mach 0.3 produced an 8x increase.

## Nomenclature

$\bar{a}$	mean axial induction	$P$	propulsion power, $W$
$\Omega_m$	motor rotational speed, $rad/s$	$Q_m$	motor torque, $N - m$
$\rho$	air density, $kg/m^3$	$R$	propeller radius, $m$
$a_t$	tangential induction factor	$r$	propeller radial position, $m$
$C_L$	wing lift coefficient	$R_0$	motor no load resistance, $ohms$
$C_r$	contraction factor of effective propeller radius	$S_{ref}$	aircraft wing reference area, $m^2$
$cl$	local coefficient of lift	$s_{TO}$	takeoff rolling distance, $m$
$D_{prop}$	propeller diameter, $m$	$T$	propeller thrust, $N$
$I_0$	motor no load current, $amps$	$v$	propeller tangential induced velocity, $m/s$
$K_v$	motor rotational constant, $rad/s$	$V_y$	propeller tangential incoming velocity, $m/s$
$m$	aircraft mass, $kg$	$V_\infty$	freestream velocity, $m/s$
$m_{motor}$	motor mass, $kg$	$w$	weight, $N$
		$x_w$	distance from rotor plane to wing, $m$

## 1. Background

In early aircraft design, distributed propulsion was more out of necessity than deliberate choice. Designs such as the Dornier Do X in 1929, the Hughes H-4 Hercules in 1947, and many other large aircraft before

\*Masters Student, Department of Mechanical Engineering, AIAA Student Member

†Assistant Professor, Department of Mechanical Engineering, AIAA Senior Member

the jet age, were constrained by the available propulsion units of the time.<sup>1</sup> With the dawn of the jet age, larger engines began to dominate design, however, some distributed and blended wing jet concepts were explored in as early as 1954.<sup>2</sup> During the push for high altitude long endurance (HALE) design, distributed electric propulsion (DEP) emerged as a viable option with NASA's Pathfinder 1983.<sup>3</sup> In 1988, NASA produced several concepts including distributed propulsion with the intention of lift augmentation<sup>4</sup> while the Pathfinder project evolved into the very similar Helios until it's destruction in 2003.<sup>5</sup> In 2014, NASA partnered with Joby Aviation and Empirical Systems Aerospace to test the Leading Edge Asynchronous Propeller Technology (LEAPTech) as a test bed for distributed propulsion research<sup>a</sup>. In June of 2016, NASA announced the X-57 Maxwell with goals to reduce the energy required for cruise by 5x at a speed of 175 mph<sup>b</sup>.

There are three main theoretical benefits associated with DEP: First, with the option to vary the size and spacing of propeller units, system tradeoffs such as higher specific power components, redundancy, and structural load distribution can be exploited.<sup>6</sup> Second, the propulsion can be directed to fill in the wing wake thus reducing drag and increasing propulsive efficiency.<sup>7</sup> Third, DEP can augment lift during takeoff and landing and also can fold the inboard propellers to enable flight with a wing specifically optimized for cruise speeds.<sup>8</sup>

The specific energy density for most electric storage systems is about 1/8 that of the effective storage for a fossil-based fuel after conversion to mechanical power. However, with that energy capacity, the range of an electric aircraft could cover over 77% of on-demand charter aviation trips.<sup>6</sup> DEP has other possible advantages such as lower system cost due to the use of smaller, more easily interchangeable power system parts, passive load alleviation from gusts due to the increased relative velocity over a wing, and enhanced safety through redundancy.<sup>9</sup>

Recent work on propeller and wing interaction has shown that a total drag reduction of over 30% can be achieved by optimizing the wing chord and twist distributions behind a given propeller.<sup>10</sup> Another study that focused on single, as opposed to distributed, propeller on wing interaction was able to show a 5% fuel savings by simultaneously optimizing both the propeller and wing.<sup>11</sup> Both of these studies coupled blade element momentum models of propellers with vortex lattice methods of wings to predict propeller on wing interactions. Specifically regarding the tangential, or swirl velocity, induced by the propeller, it is important to note that not all of this velocity is applied to the boundary condition in the vortex lattice method.<sup>12</sup> Neglecting a correction on the swirl velocity over-predicts its effect on the wing lift distribution as previously noted.<sup>13</sup> Additionally, the optimal blown lift distribution is non-elliptical,<sup>14</sup> which makes the propeller on wing interaction critical for wing design in a propeller wake.



Figure 1: Illustration of the NASA X-57 concept aircraft showing the mid span DEP propellers in the folded cruise position.

Similar to the results presented in our study, the NASA X-57 is designed to augment the lift of a wing to enable a design better suited for cruise, without sacrificing takeoff and landing performance. Researchers from NASA and Joby Aviation have found that by using all of the propellers during takeoff and landing, the dynamic pressure difference on the wing is increased at low speeds and produces an effective lift coefficient of

<sup>a</sup>NASA Leaptch [nasa.gov/centers/armstrong/Features/leaptch.html](https://nasa.gov/centers/armstrong/Features/leaptch.html), accessed 12/14/17

<sup>b</sup>NASA Leaptch [nasa.gov/press-release/nasa-electric-research-plane-gets-x-number-new-name](https://nasa.gov/press-release/nasa-electric-research-plane-gets-x-number-new-name), accessed 12/14/17

about five. In cruise, when the center propellers are folded and inactive, the aircraft achieves an estimated 82% increase in lift over drag as compared to the baseline Cirrus SR22.<sup>8</sup> Our study differs in that we: First, explore the effects of requiring all of the propulsion units to be in use for the entirety of the modeled flight. Second, analyze a broad range of numbers of propellers. Third, include power system effects on mass and efficiency. Fourth, investigate the effects of required range and propeller tip speed constraints through optimization. We hope to help bridge the work of the studies on propeller on wing interaction with the work on DEP to aid in the push to make commercial electric propulsion a reality.

## 2. Model Description

### 2.1. Propeller Performance

#### 1. Blade Element Momentum Theory

CCBlade is an open source blade element momentum (BEM) code originally designed for wind turbine analysis,<sup>15</sup> but which has been extended for propeller analysis including all possible inflow angles, large axial inductions, yawed inflow, hover, and non-rotating blades. From CCBlade we extract axial and tangential

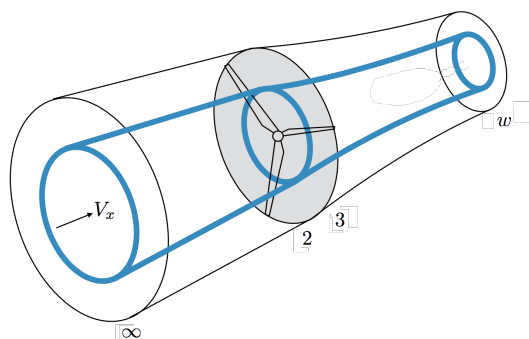


Figure 2: The blue streamtube depicts an annular control volume used in blade element momentum theory.

flow distributions to compute the influence on the wing. Based on strip theory, BEM calculates the axial and tangential induction factors for each annular disk of the propeller (Fig. 2) including hub and tip loss correction factors.<sup>16</sup> Propeller wakes generally reach their far-field values within approximately one rotor radius, and in these studies we assume that the wing is sufficiently far from the propeller for far-field values to be reasonably accurate. In the far-field, the induced velocities are double what they are at the rotor plane. Additionally, as previously shown<sup>17, 10</sup> not all of the tangentially induced velocity from the propeller is applied normal to the wing. This reduction, or swirl reduction factor (SRF), is approximately 0.5<sup>17</sup> for small angles of attack.

Calculating the slipstream contraction includes a simple momentum balance between the flow rate at rotor station 3 and the far wake  $w$  as seen in Fig. 2. We assume that the annular contraction is fixed at the wake center and the contraction compounds until the edge of the stream tube. Although we include this slipstream contraction, we assume the the far wake is developed before encountering the wing and we assume that the propeller slipstream does not go above or below the wing. Therefore, we can assume slipstream contraction effects on wing relative angle of attack are negligible. The equation for the annular area contraction including axial induction<sup>17</sup> can be see in Eq. (2), where a mean axial induction is used as shown in Eq. (1).

$$\bar{a} = \text{mean}\left(\frac{u}{V_x}\right) \quad (1)$$

$$C_r = \sqrt{\frac{1 + \bar{a}}{1 + \bar{a}\left(1 + \frac{x_w}{\sqrt{R^2 + x_w^2}}\right)}} \quad (2)$$

Rotational airfoil data across a range of angles of attack, Reynolds number, and Mach number is acquired by using XFOIL data corrected by AirfoilPrep.py.<sup>18</sup> Airfoilprep.py applies a rotational correction and extrapolation to high angles of attack. In this study only propeller diameter is changed, with chord and thickness scaling with diameter. The mass of the propellers is estimated as a solid propeller with a density of  $1440 \text{ kg/m}^3$  for carbon fiber prepreg, similar to propellers manufactured by Warp Drive Propellers<sup>c</sup>.

## 2.2. Wing Performance

### 1. Vortex Lattice Method

The vortex lattice method (VLM) is a discretized lifting line theory that calculates the inviscid lift and lift-induced drag for non-uniform freestream and geometry.<sup>19,20</sup> Typically the method is implemented with a uniform freestream that is applied independently at each vortex boundary condition. In order to account for the propeller on wing effects, we have included the propeller axial and tangential velocity distributions in the boundary condition similar to that done by Veldhuis.<sup>17</sup> This VLM was developed and validated previously for formation flight studies, for which similar wake-wing interactions exist.<sup>21</sup>

The current models differ from Veldhuis' work with the following assumptions: First, the propeller slipstream will not be above or below the wing. Second, the propellers are far enough removed from the wing so that wing on propeller interactions are negligible. Third, viscous, or parasitic drag, is modeled using strip theory and XFOIL 2D values for a given angle of attack, Mach number and Reynolds number. To account for the wing viscous drag in the propeller wake, we assume fully turbulent transition and run XFOIL with a forced transition at the airfoil leading edge. To speed up the optimization process, we precompute these values and use a three dimensional cubic interpolation method which returns continuously differentiable outputs. Section 3 contains the comparison results of our model and the experimental data collected by Epema.<sup>10</sup>

While vortex lattice methods can be evaluated rapidly, their discrete panels can create difficulties with gradient-based optimization. This problem arises for this study because we are interested in exploring different propeller sizes. As the propeller diameter changes, the propeller wake blankets a different number of VLM panels. Specifically, as the wake moves over a new control point, the predicted forces and moments change in a discontinuous manner. One possible solution is to evaluate discrete quantities of rotor diameters, but this creates a larger combinatorial problem with the number of propellers and greatly increases evaluation time. Instead, we seek an approach where the rotor diameter can be directly used in gradient-based optimization without the nonphysical noise.

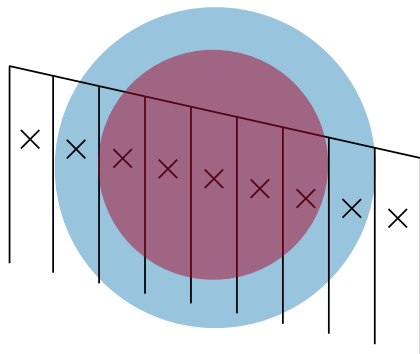


Figure 3: A representation of the strategy used to evaluate changing rotor diameters. The red and blue circle represent the nearest diameters surrounding the actual wake diameter while covering a whole number of panels exactly. The smoothing strategy requires evaluating both of these nearby diameters and then linearly interpolating the vortex lattice outputs to the actual diameter.

Our methodology has two parts. First, we ensure that the center of the propeller wake is centered on a wing control point. Because the position and number of propellers are fixed during the optimization, these

<sup>c</sup>Warp Drive Propellers Inc. Commercial Website [warpdriveinc.com](http://warpdriveinc.com), accessed 12/9/17

locations can be precomputed. Second, for each wake diameter we find the two nearest diameters, one smaller and one larger, that exactly cover full panels (see Fig. 3). We evaluate the VLM at both conditions, then linearly interpolate the VLM outputs using the wake diameter (this is not the same as the rotor diameter because of wake contraction). A comparison of the unmodified diameter sweep, and the modified diameter sweep is shown in Fig. 4. The original function contains many artificial local minimum, while this modified approach produces a differentiable output. While this modification does require twice the number of function calls to the VLM, it allows for rotor diameter to be directly included in the optimization which greatly reduces the number of function calls required for optimization and improves convergence robustness.

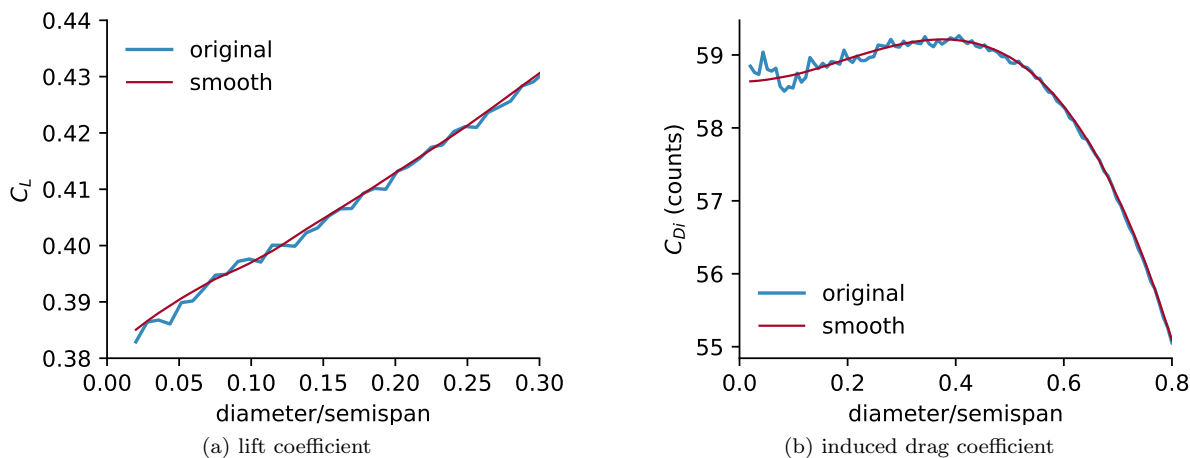


Figure 4: A comparison between the original VLM output and our modified approach with changing rotor diameter. As the propeller diameter changes the propeller wake discrete intersects with wing control points creating noisy output. Our modified approach allows for smooth variations with changing propeller diameter. The lift coefficient is shown on a smaller x-axis range because the oscillations are smaller and are harder to see when zoomed out.

## 2.3. Power System

### 1. Electric Motor

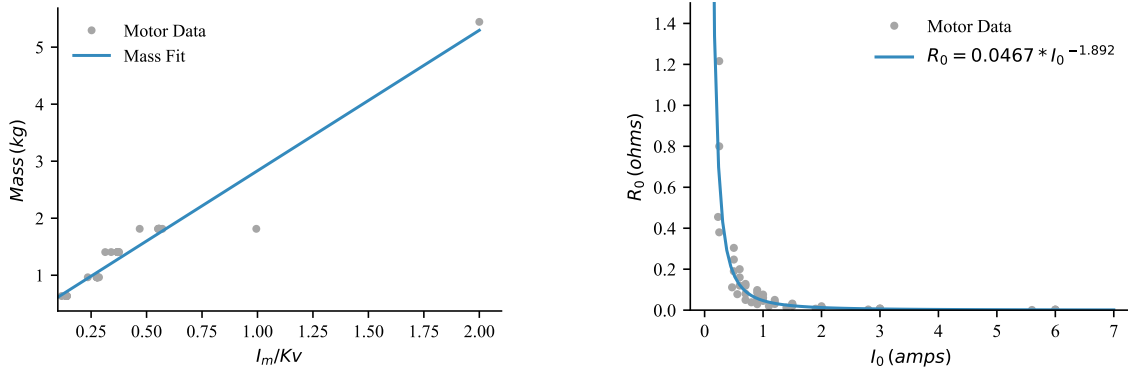
For calculating motor efficiency and power, we use a fundamental first order motor model.<sup>22</sup> The parameters used in the model include the rotational speed constant  $K_v$ , the no-load current  $I_0$ , the no-load resistance  $R_0$ , torque  $Q_m$ , and rotational speed  $\omega_m$ . This model assumes no losses due to increased resistance from heating. A second order model that does include these effects is also available by the same author,<sup>23</sup> but requires heat transfer modeling. Comparing the first order model to the Maxon 305013 Brushless Motor data, we found the efficiency, current, and required voltage to all be within 1.5% for the nominal RPM and torque.

In order to model the motor mass, we created a fit to the motor data from the Astroflight<sup>e</sup> line of motors. Astroflight motors were chosen due to the availability of data and the favorable range of both power and  $K_v$ . We found a linear relation between the mass and the motor peak current divided by the motor  $K_v$  parameter (Fig. 5a). This reduces to electric power/RPM where this power is the motor electrical power under load. If we assume no efficiency losses, this term further reduces to torque. The line fit in Eq. (3) shows the trend of the best motors and is used in estimating the motor mass. The motors included in this empirically based model powers ranged from 1.5 kW to 15 kW and  $K_v$  from 32 to 1355.

$$m_{motor} = 2.464 I_m / K_v + 0.368 \quad (3)$$

<sup>d</sup>Maxon Motors Online Catalog [www.maxonmotorusa.com](http://www.maxonmotorusa.com), accessed 12/9/17

<sup>e</sup>Astroflight Brushless Motors [astroflight.com/motors/brushless-motors](http://astroflight.com/motors/brushless-motors), accessed 12/9/17



(a) Motor mass model using Astroflight motor data. The equation for the linear fit is shown in Eq. (3).

(b) Motor  $I_0$  and  $R_0$  follow Eq. (4).

Figure 5: Data fits based on Astroflight motor data.

To accurately model motor performance in addition to mass, we investigated the relationship between all of the motor parameters. We found that there were no interdependencies other than those between the mass, motor peak current, and  $K_v$ , and between the no-load resistance and no-load current. The trend for the latter can be seen in Fig. 5b and the accompanying fit in Eq. (4) which follows the inverse relationship of Ohms Law.

$$R_0 = 0.0467(I_0)^{-1.892} \quad (4)$$

## 2. Motor Controller

The motor controller model for mass was assumed to be linear based on the specific power of 22,059 W/kg taken from the Astroflight high voltage motor controller.<sup>f</sup> Efficiency was assumed to be a constant 97% due to a lack in motor controller data.

## 3. Battery

The battery was modeled with a specific energy parameter of 300 Wh/kg. We have not included the second order effects of current draw on cell voltage.

## 2.4. Takeoff Ground Roll Distance

Similar to turbine engine based propulsion where thrust is relatively constant, electric propulsion power is relatively constant. Because of this, a slight variation in the takeoff rolling distance is required. Beginning with the the same assumptions as Anderson<sup>24</sup> in his takeoff performance equation, we modify the derivation to assume a constant power during takeoff resulting in the following integration for takeoff roll distance:

$$s_{TO} = \frac{mV_{\infty}^3}{3P\eta_p} \quad (5)$$

For battery sizing, we also use the ground roll distance time at constant power in Eq. (6).

$$t_{TO} = \frac{mV_{\infty}^2}{2P\eta_p} \quad (6)$$



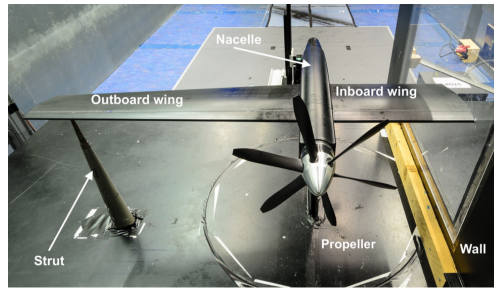


Figure 6: Propeller wing test model used by Epema.<sup>10</sup> Test model included pressure ports distributed across the wing surfaces to measure local pressure distributions.

### 3. Propeller on Wing Validation

#### 3.1. Propeller Performance Comparison

To validate that the BEM code with XFOIL airfoil data calculation was consistent with Epema's published experimental cases, we extracted the propeller geometry from the figures in his report. Using the chord, twist, and airfoil data, we ran XFOIL for the calculated Reynolds and Mach numbers along the blade then calculated the thrust and torque at a constant RPM. As can be seen in Fig. 7, the results match reasonably well. Because of some uncertainty in the exact geometry, the blade pitch is adjusted until the thrust coefficient of the propeller matches that reported in the respective studies. Overall, excellent agreement is observed in the propeller thrust and efficiency.

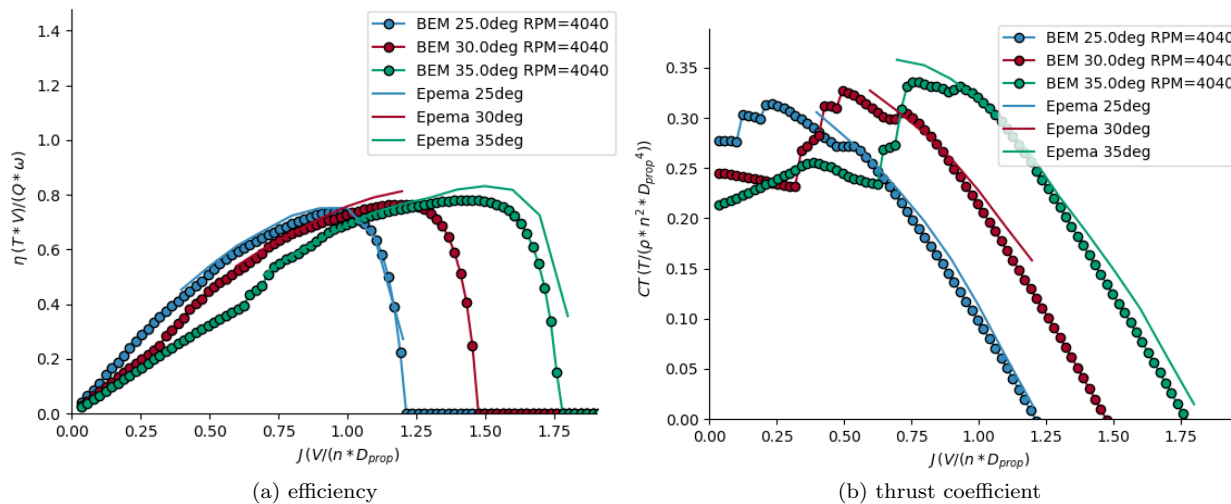


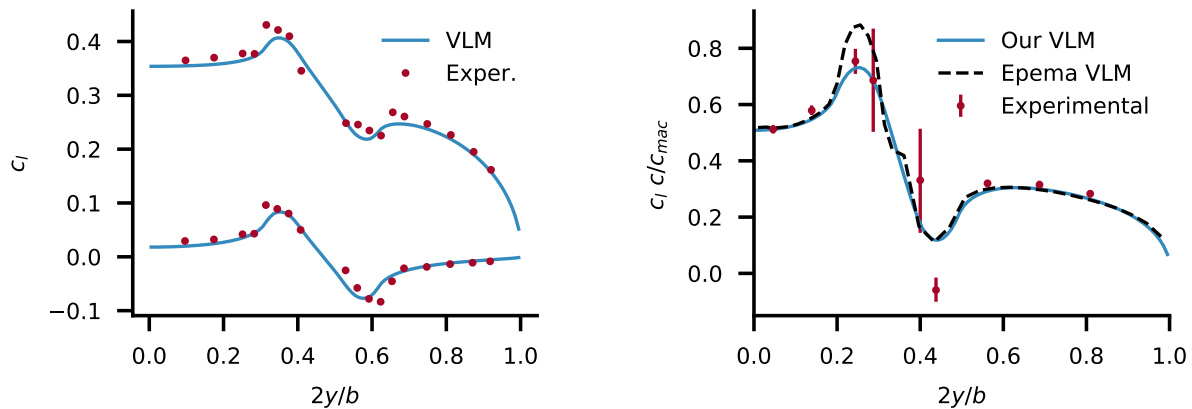
Figure 7: Comparison of efficiency and thrust data collected by Epema<sup>10</sup> and the BEM code using XFOIL airfoil data.

#### 3.2. Local Lift Coefficient Comparison

We examined two separate validation cases for the propeller on wing interaction. The first case is from wind tunnel data of a single propeller on a straight untwisted wing.<sup>14,17</sup> Data is available at two angles of attack:  $0^\circ$ , and  $4^\circ$ . Figure 8a shows a comparison between the experimental lift coefficient and that predicted by our methodology for both angles of attack. Excellent agreement is observed.

The second set of experiments comes from a separate wind tunnel experiment with a larger propeller and a tapered wing.<sup>10</sup> We compare the results for the lift distribution for our VLM, the VLM developed

<sup>f</sup>Astroflight Motor Controller [astroflight.com/esc-2413](http://astroflight.com/esc-2413), accessed 12/9/17



(a) lift coefficient distribution from our BEM/VLM compared to experimental wind tunnel data at two angles of attack

(b) lift distribution from our BEM/VLM compared to Epema VLM and experimental data

Figure 8: Two validation cases for propeller on wing interaction using two different geometries.

by Epema in that same study, and the wind tunnel data. Reported error bars in the wind tunnel data are included in Fig. 8b. The two VLMs agree very closely except where the propeller swirl velocity induces wing upwash. In this region our VLM more closely matches the experimental data.

## 4. Optimization Setup

The objective of the optimization is to minimize the takeoff rolling distance assuming constant power and efficiency while constraining the cruise range of the aircraft. Additional constraints are added on stall, takeoff lift, thrust, propeller separation, tip Mach number, and flight time. These constraints are shown in Fig. 9 along with a visual representation of the optimization framework, which is designed to be relatively simple, robust, and continuously differentiable.

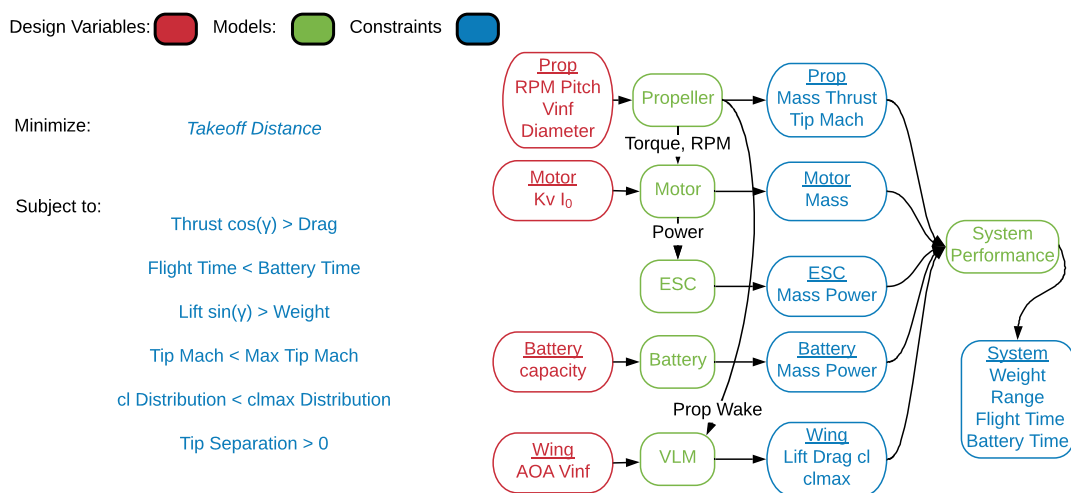


Figure 9: Optimization framework with design variables in red, models in green, and outputs in blue. For the multi objective optimization of takeoff distance and range, we added a range constraint and ran the analysis framework twice with additional variables for angle of attack, pitch, RPM, and velocity for both cruise and takeoff conditions.



To account simply for the climb and takeoff portions of the flight, we assumed that landing would require approximately the same power as takeoff and that the rolling distance was 60% of the takeoff field length<sup>8</sup>. We also added a cruise range reserve of 20%.

We use SNOPT,<sup>25</sup> a gradient-based sequential quadratic programming method designed for large scale constrained optimization, for the optimization algorithm. For our results, we calculate gradients using finite differencing, and scale design variables and constraints so that the gradients are approximately of order 1.

#### 4.1. Baseline Aircraft

As an example of a typical modern short haul commuter aircraft, we chose the Cirrus SR22 which has been used by the LEAPTech studies,<sup>8</sup> was certified relatively recently, and has a large number of units in operation. Table 1 shows the main design parameters of the aircraft.

Table 1: Baseline Cirrus SR22 aircraft<sup>26</sup>

Parameters	Cirrus SR22
Cruise Speed	94.3 m/s
Gross Weight	1542 kg
Wing Area	13.47 m <sup>2</sup>
Wing Span	11.67 m
Aspect Ratio	10.1

## 5. Results Analysis

### 5.1. Range Constraint Sweep

In this study, we explore tradeoffs between takeoff distance and range for the general parameters of the baseline aircraft, but with continuously powered distributed propellers and a variable aspect ratio wing. We chose a battery specific energy of 300 Wh/kg, typical of current battery technology, a payload and structural mass of 1,000 kg not including the propulsion and batteries, a propeller tip speed constraint of Mach 0.8 for noise and compressibility constraints, and variable pitch propellers for takeoff and cruise. This configuration, though possibly less optimal than the NASA X-57 optionally power propulsion units, does not include any discrete design variables other than number of propellers. This enables gradient-based optimization and scalability in terms of design variables.

Using our optimization framework, we investigate only the effects of the propulsion and wing, while assuming trim drag and fuselage forces to be negligible for this comparative study. We vary the propeller number ranging from 2 to 32, set up the VLM model with 100 control points, and use the same propeller geometry as the validation case, but with 2 blades, pitch as a design variable, and geometric scaling with radius. In order to model both takeoff and cruise performance, we double the variables of RPM, pitch, angle of attack, and battery capacity for both takeoff and cruise. We use only one set of variables for the propeller radius and motor parameters and size the electronics based on the higher-power takeoff case.

We have implemented the optimization framework in the Julia programming language with excellent computational efficiency. The full propeller and wing analysis runs in an average of approximately 0.6 seconds. This means full optimizations usually converge on the order of minutes when starting at a random point.

Keeping in mind that we are only directly modeling and reporting the takeoff rolling distance and not the full required takeoff field length, Fig. 10 shows that a greater blown fraction of the wing shortens the takeoff rolling distance in excess of 75% when compared to the 2 propeller case. There are two main factors in play that enable such short takeoff rolling lengths.

The first main factor contributing to such a short takeoff distance is total thrust. The total thrust being generated is in some cases is greater than the weight of the aircraft (Fig. 11). This is due to the relatively

<sup>8</sup>Pilot Guide to Takeoff Safety [www.faa.gov](http://www.faa.gov), accessed 12/9/17

large propeller area as well as the inclusion of variable pitch propellers, which enables much higher thrust at low speeds. This high thrust is also possible due to the short time required for takeoff, where the large power required to generate such a massive amount of thrust does not significantly contribute to the battery mass. Even for the short range 32 km case, the time for takeoff and landing as described in Section 4 is less than 0.08% of the cruise time. Coupling the time with the power, the 32 km case consumed 10x the power in takeoff over cruise, which puts the takeoff portion of battery capacity at less than 1.0% of the total battery mass. Additionally, electric power systems have the advantage of very high power to weight components, despite the relatively low energy density of the batteries, which enables grossly oversized motors to be used without much penalty in mass.

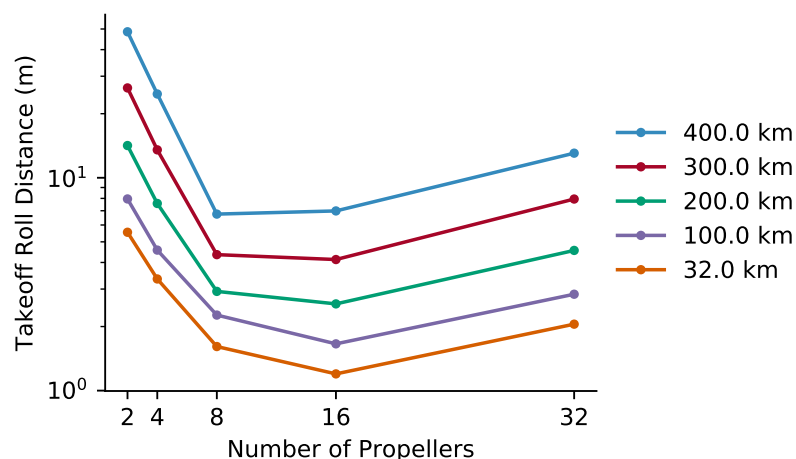
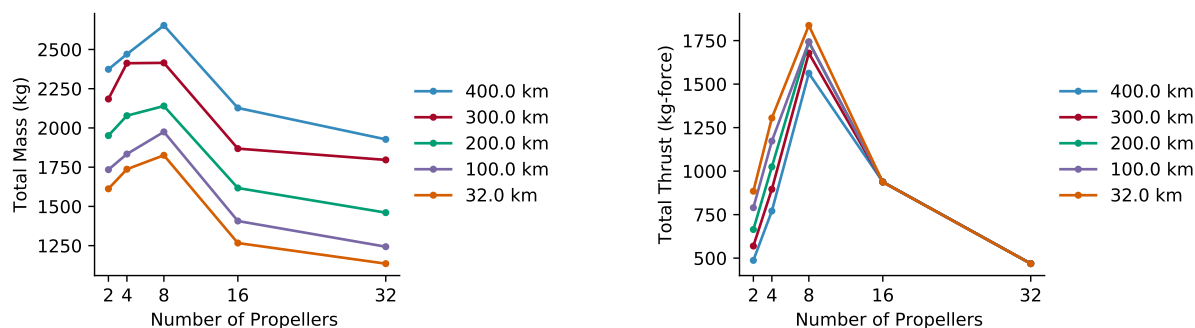


Figure 10: Increasing propellers yields favorable better takeoff performance for ranges less than 500km.

Figure 12a gives a visual description of the full wing span and number of propellers, in addition to the optimal propeller diameter for a range constraint of 32 km. Above 8 propellers, the blades were effectively tip to tip across the span with the maximum diameter constraint active. With increasing range constraints, the optimal diameter tradeoff between takeoff and cruise conditions becomes more heavily weighted towards the cruise conditions. In this case, the propeller diameter decreases with increased range (Fig. 12b).



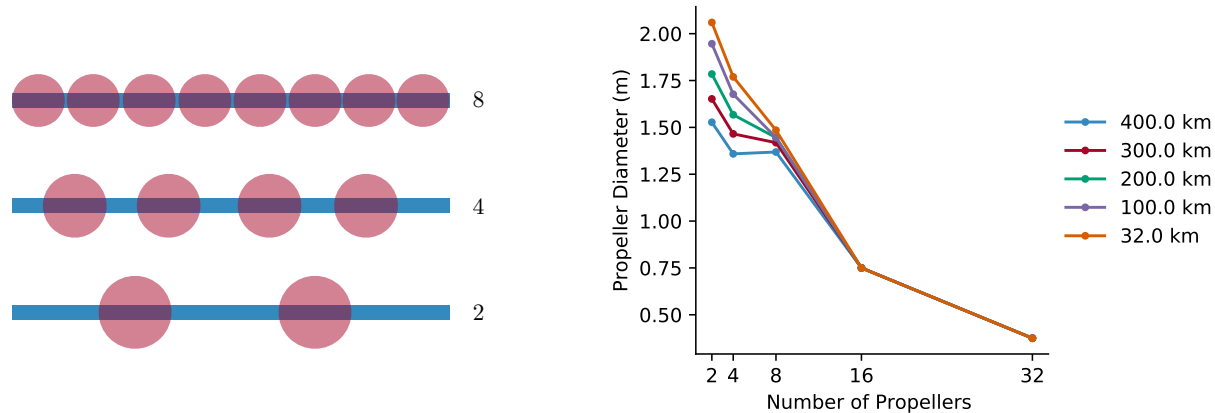
(a) Mass of the aircraft is similar to baseline mass when the propulsion and power systems are included

(b) A fully blown configuration with unconstrained propeller diameter and rotational rate produces the greatest thrust.

Figure 11: Total thrust at takeoff is in some cases greater than the aircraft weight.

After 8 propellers on the span, the takeoff rolling distance increases due to the thrust limitations. The propeller tip separation and Mach constraints are active, which limits both the diameter and rotational speed. Our optimization does not include variable propeller chord or airfoil type, and so increasing pitch is the only other way to increase thrust. At high pitch the propellers are subject to stall and thus the possible thrust is at the upper limit as seen in Fig. 11b. Also of interest in Fig. 12b is the variation of propeller diameter with respect to the range constraint. If we were to run optimizations for different numbers of

propellers between 8 and 16, we might find a different optimal number of propellers based on the optimal propeller diameter for a given range constraint.

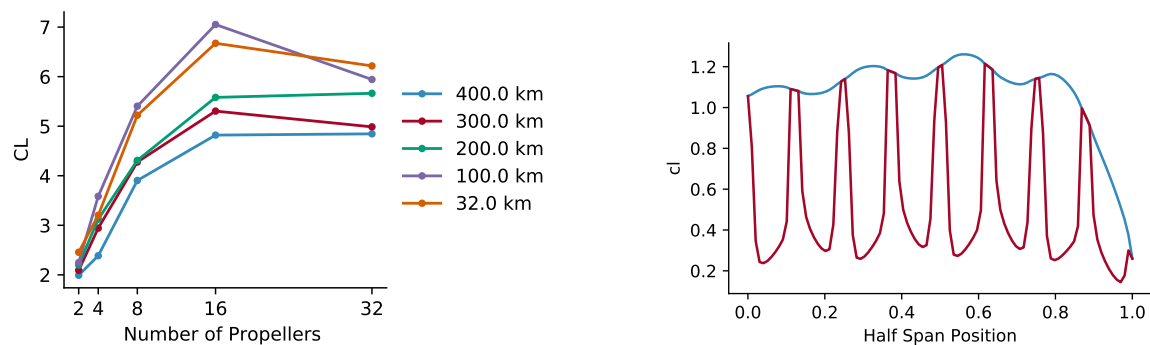


(a) Visual depiction of optimal rotor diameters relative to wing span. For 8 propellers or more, the blades are effectively tip-to-tip across the span.

(b) Propeller diameter decreases with increased range requirements except in the cases where the optimal diameter is larger than permitted.

Figure 12: Perspective of optimal propeller diameter with respect to wing span, range constraint, and number of propellers.

The second main factor contributing to such a short takeoff distance is decreased stall speed due to an augmented wing lift coefficient as seen in Fig. 13a. Considering a lower stall speed in addition to the high thrust at takeoff, the time to accelerate the aircraft to the takeoff speed is lowered even more. We also include thrust vectoring where a component of the propeller thrust contributes to lift as the angle of attack is increased, at the cost of decreased forward thrust. With the high amount of thrust being produced at takeoff, the tradeoff between thrust and lift isn't an issue. The decrease in stall speed, not including vectored thrust, is accomplished by the propellers increasing the dynamic pressure on the wings. The local lift coefficient, normalized by the local velocity, remains below the specified stall constraint of 1.2 even during angles of attack in excess of 30 degrees. Figure 13b shows an example of this.



(a) Fully blown configurations increase wing total lift coefficient as normalized by the freestream, though for diameter and rotational speed constrained propellers, blown velocities and in turn lift coefficient is also constrained

(b) Local (red) and freestream (blue) normalized lift coefficient distributions show significant decrease in the local lift coefficient which integrates to an augmented wing freestream normalized lift coefficient. The local lift coefficient max constraint was set at 1.2, range constraint was 300 km, and number of propellers was 8.

Figure 13: Blown configurations generate a significant increase in wing total lift coefficient by decreasing the local velocity normalized lift coefficient.

On a side note, since we calculate wing parasitic drag using a strip method and XFOIL, we had the option to assume a fully turbulent wing, or allow laminar transition. We assumed that the portions of the wing inside the propeller wake were fully turbulent and the sections outside of the wake to have a free transition. We ran the analysis including fully turbulent airfoil data everywhere as opposed to a mix of free transition and fully turbulent, but found only a small change in the objective takeoff field distance.

## 5.2. Propeller Tip Speed Constraint Sweep

For new aircraft to be of value as defined by NASA, noise is a key element.<sup>6</sup> While we have not modeled noise production in the analysis framework presented in this paper, the propeller tip speed can be treated as a surrogate for noise. For all of the cases tested in Section 5.1, the takeoff tip speed constraint was active at the specified Mach 0.8, indicating that decreasing the noise requirements, or propeller tip speed, will affect the design and performance. For this study, we take a nominal range, 300 km, with all of the same parameters and design variables as before, but sweep the Mach number constraint from 0.8 down to 0.3. Below Mach 0.3, many of the design cases were infeasible and are not included in this comparative study.

Figure 14 shows the effect of the propeller tip speed constraint on the takeoff distance for all of the numbers of propellers tested. For the 8 propeller case, there is an 8x increase in the takeoff roll distance between propeller tip speeds of Mach 0.8 and Mach 0.3. However, the trend in increasing takeoff distance seems to be exponential, with only a 1.5x increase between tip speeds of Mach 0.8 and Mach 0.6. This exponential trend indicates that there may be a possibility to significantly decrease noise with little impact on takeoff performance.

In Figure 14, there appears to be some multi-modality in some solutions for the 2 propeller case. The Mach 0.6 case outperforms the Mach 0.8 case which is contrary to the trends suggested in the rest of the results. For a starting diameter, the optimization may get caught in a local optimum using a rotational rate and diameter for which the tip speed constraint is active. By changing the initial conditions, the optimization may converge on another diameter and rotational rate. To overcome this, we may need to include a multi-start scheme in our future optimization framework.

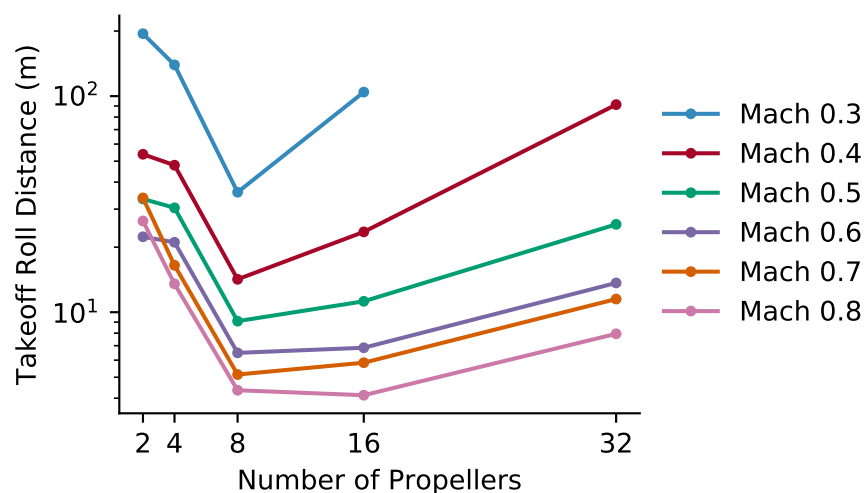
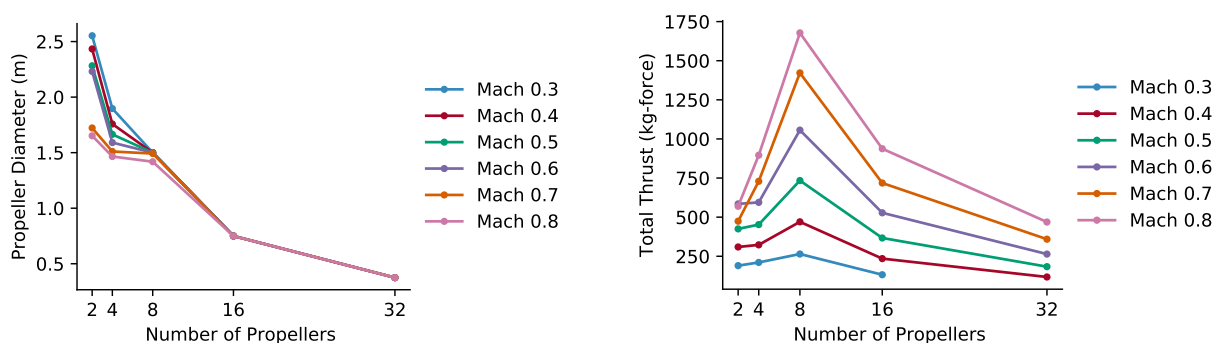


Figure 14: Decreasing the propeller tip speed constraint significantly decreases takeoff distance. This analysis differs from Section 5.1 with a fixed 300 km range constraint and varying propeller tip speed constraint.

To go further into the effects of the tip speed constraint, we focus on the two main factors that decrease takeoff field length in Section 5.1: thrust and lift coefficient. First, the propeller tip speed directly affects the rotational rate. To make up for this, the optimizer tends to choose a larger propeller until limited by the tip separation constraint. This can be seen in Fig. 15a for the 8 propeller case where the diameter maxes out at just above 1.5 m for tip speeds of Mach 0.7 and above. With the propeller diameter and rotational rate constrained, the pitch will become maxed out, and the possible thrust cannot be increased. Figure 15b shows this clearly with the Mach 0.3 case significantly decreasing the relative difference in thrust between the 8 propeller and 2 propeller cases. Additionally, with decreased available thrust, the effects of thrust

vectoring described previously for high angles of attack are also diminished. This increases the stall speed, as well as the time to accelerate the aircraft mass to takeoff speed.

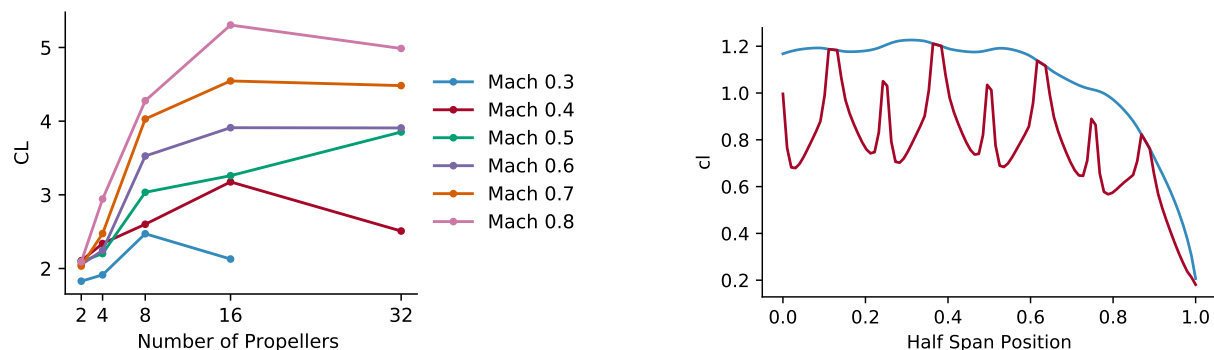


(a) Propeller diameter grows with decreasing tip speed constraint until the propellers become tip to tip.

(b) Available takeoff thrust is diminished with decreasing maximum tip speed.

Figure 15: Mach number constraint pushes propeller diameter to the upper bound and decreases available thrust at takeoff.

Second, with the decrease in available thrust due to the tip speed constraint, the propeller wake velocity is also decreased. This decreases the dynamic pressure relative to a case with a higher blown velocity, and in turn, decreases the wing lift coefficient. As seen in Fig. 16a for the 8 propeller case, the lift coefficient is decreased from 4.2 at Mach 0.8 to 2.4 at Mach 0.3. Looking at the local lift coefficient for this case in Fig. 16b, the local velocity normalized lift coefficient is much lower than the Mach 0.8 case shown in Fig. 13, which in turn integrates to the lower total wing lift coefficient.



(a) Fully blown configurations increase wing total lift coefficient, though for diameter and rotational speed constrained propellers, blown velocities and in turn lift coefficient is also constrained.

(b) Local (red) and freestream (blue) normalized lift coefficient difference for tip speed constraint of Mach 0.3 is much less than in Fig. 13. This integrates to a lower total wing lift coefficient. The max local lift coefficient constraint was set at 1.2, range constraint at 300 km, and number of propellers at 8.

Figure 16: Decreased propeller thrust, and in turn decreased wake velocity, decrease the difference in local and freestream normalized local lift coefficient.

With decreased available thrust and decreased wing lift coefficient, it takes longer to accelerate the aircraft mass to a higher takeoff speed than before. However, as previously mentioned and as shown in Fig. 17, this trend is exponential showing relatively little effect on the takeoff rolling distance until the tip speed constraint of Mach 0.5. As a surrogate for noise, this study on propeller takeoff tip speed could indicate significant opportunities for noise reduction while leaving the takeoff performance relatively unaffected.

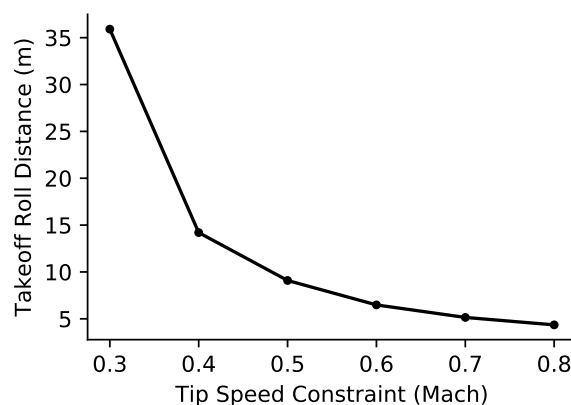


Figure 17: Takeoff distance for the 8 propeller case with varying tip speed constraint shows relatively small effect on performance for tip speed constraints between Mach 0.8 and Mach 0.5. Range constraint was 300 km.

## 6. Conclusions

In this paper, we explore how continuously powered distributed propulsion can reduce takeoff distance while maintaining a variety of range constraints. We use a variety of validated models including blade element momentum methods, vortex lattice methods, experimental data, and nonlinear optimization techniques to model and explore the design space. We have found that for this conceptual design study, a fully blown wing with propellers at the optimal diameter for the load (8 propellers for a 300 km range constraint in this study) can reduce the takeoff distance by over 80% when compared to the optimal 2 propeller case using the same models. There is over a 2x increase in the wing lift coefficient which leads to a 36% reduction in liftoff speed. Also, the optimal fully blown case produced 2.9x more thrust during takeoff over the 2 propeller case with only an 11% increase in total aircraft mass. Using propeller tip speed as a surrogate for noise, we found that the propeller tip speed decreased takeoff performance in an exponential manner: the tip speed could be decreased from Mach 0.8 to Mach 0.5 with only a 2x increase in takeoff rolling distance while decreasing the constraint to Mach 0.3 produced an 8x increase. By continuing to exploit the strengths of electric propulsion through increased takeoff thrust and decreased wing stall speed, the limits of aircraft design can be pushed to help make electric aircraft an everyday reality.

Future work will focus on exploring a greater number of design sensitivities to things like propeller and wing structures, different mission profiles, various battery technologies, and a more in depth study on propeller noise. Additionally, future improvements will include adding analytic gradients to the models, improving the parasitic drag model, including the influence of the wing on the propellers, including the influence of closely spaced propellers, calculating the swirl recovery factor for propeller tangential velocity, and including non-normal inflow to the propeller.

The final code and data used to produce this report will be available on the BYU FLOW Lab website (<http://flow.byu.edu/publications/>) following a brief embargo period.

## Acknowledgments

The authors gratefully acknowledge support from The Connectivity Lab at Facebook. Design choices, findings, and conclusions are those of the authors and do not necessarily reflect the views of Facebook.

## References

- <sup>1</sup>Gohardani, A. S., Doulgeris, G., and Singh, R., "Challenges of future aircraft propulsion: A review of distributed propulsion technology and its potential application for the all electric commercial aircraft," *Progress in Aerospace Sciences*, Vol. 47, October 2011, pp. 369–391.
- <sup>2</sup>Griffith, A., "Improvements relating to aircraft and aircraft engine installations." United Kingdom Patent, 720,394, 1954.
- <sup>3</sup>Flittie, K. and Curtin, B., *Pathfinder solar-powered aircraft flight performance*, American Institute of Aeronautics and



Astronautics, 2017/12/14 1998.

<sup>4</sup>Yaros, S., Sexstone, M., Huebner, L., Lamar, J., McKinley, R., and Torres, A., “Synergistic airframe-propulsion interactions and integrations: a white paper prepared by the 1996–1997 Langley Aeronautics Technical Committee,” Tech. Rep. TM-1998-207644, NASA, 1998.

<sup>5</sup>Noll, T. E., Ishmael, S. D., Henwood, P., and Perez-Davis, M. E., “Technical Findings, Lessons Learned, and Recommendations Resulting from the Helios Prototype Vehicle Mishap,” No. 3.4, UAV Design Processes / Design Criteria for Structures, 2007, pp. 1–18.

<sup>6</sup>Moore, M. D. and Fredericks, B., “Misconceptions of Electric Propulsion Aircraft and their Emergent Aviation Markets,” No. 2014-0535 in 52nd Aerospace Sciences Meeting, Jan 2014.

<sup>7</sup>Ko, Y.-Y. A., *The Multidisciplinary Design Optimization of a Distributed Propulsion Blended-Wing-Body Aircraft*, Ph.D. thesis, Virginia Polytechnic Institute and State University, Blacksburg, Virginia, April 2003.

<sup>8</sup>Stoll, A. M., Bevirt, J., and Moore, M. D., “Drag Reduction Through Distributed Electric Propulsion,” No. 2014-2851 in Aviation Technology, Integration, and Operations Conference, June 2014.

<sup>9</sup>Leifsson, L. T., Ko, A., Mason, W. H., Schetz, J. A., Haftka, R. T., and Grossman, B., “Multidisciplinary Design Optimization for a Blended Wing Body Transport Aircraft with Distributed Propulsion,” Tech. rep., Multidisciplinary Analysis and Design Center for Advanced Vehicles, May 2005.

<sup>10</sup>Epema, H., *Wing Optimisation for Tractor Propeller Configurations*, Master’s thesis, Delft University of Technology, June 2017.

<sup>11</sup>Alba, C., Elham, A., Veldhuis, L. L. M., and German, B. J., “A Surrogate-Based Multi-Disciplinary Design Optimization Framework Exploiting Wing-Propeller Interaction,” AIAA, June 2017.

<sup>12</sup>Alba, C., Elham, A., German, B., and Veldhuis, L. L., *A Surrogate-Based Multi-Disciplinary Design Optimization Framework Exploiting Wing-Propeller Interaction*, American Institute of Aeronautics and Astronautics, 2017/12/14 2017.

<sup>13</sup>Hunsaker, D. and Snyder, D., *A Lifting-Line Approach to Estimating Propeller/Wing Interactions*, American Institute of Aeronautics and Astronautics, 2017/12/14 2006.

<sup>14</sup>Veldhuis, L. L. M., “Review of Propeller-Wing Aerodynamic Interference,” *International Congress of the Aeronautical Sciences*, 2004.

<sup>15</sup>Ning, A., “A Simple Solution Method for the Blade Element Momentum Equations with Guaranteed Convergence,” *Wind Energy*, Vol. 17, No. 9, September 2014, pp. 1327–1345.

<sup>16</sup>Glauert, H., *Airplane Propellers*, Vol. 4, Springer Verlag., 1935.

<sup>17</sup>Veldhuis, L. L. M., *Propeller Wing Aerodynamic Interference*, Ph.D. thesis, Technical University of Delft, June 2005.

<sup>18</sup>Ning, S., *AirfoilPrep.py Documentation*, NREL, 1st ed., Sept 2013.

<sup>19</sup>Katz, J. and Plotkin, A., *Low speed aerodynamics – From wing theory to panel methods*, No. ISBN 0-07-050446-6, Mc. Graw-Hill, 1991.

<sup>20</sup>Bertin, J. J., *Aerodynamics for engineers*, No. ISBN 0-13- 064633, Prentice Hall, 4th ed., 2002.

<sup>21</sup>Ning, A., Flanzer, T., and Kroo, I., “Aerodynamic Performance of Extended Formation Flight,” *Journal of Aircraft*, Vol. 48, No. 3, May 2011, pp. 855–865.

<sup>22</sup>Drela, M., *First Order DC Electric Motor Model*, MIT Aero and Astro, Cambridge Massachusetts, February 2007.

<sup>23</sup>Drela, M., *Second Order DC Electric Motor Model*, MIT Aero and Astro, Cambridge Massachusetts, February 2007.

<sup>24</sup>Anderson, J. D., *Introduction to Flight*, Mc. Graw-Hill, 6th ed., 2008.

<sup>25</sup>Gill, P. E., Murray, W., and Saunders, M. A., “SNOPT: An SQP algorithm for largescale constrained optimization,” *SIAM Journal on Optimization*, Vol. 12, No. 4, 2002, pp. 979–1006.

<sup>26</sup>“Airplane Information Manual for the Cirrus Design SR22,” Cirrus Aircraft, 4515 Taylor Circle, Duluth, MN 55811, September 2011.